

Dynamics and Trajectory Optimization for a Soft Spatial Fluidic Elastomer Manipulator

Andrew D. Marchese, Russ Tedrake, and Daniela Rus*

May 13, 2015

Abstract

The goal of this work is to develop a soft robotic manipulation system that is capable of autonomous, dynamic, and safe interactions with humans and its environment. First, we develop a dynamic model for a multi-body fluidic elastomer manipulator that is composed entirely from soft rubber and subject to the self-loading effects of gravity. Then, we present a strategy for independently identifying all unknown components of the system: the soft manipulator, its distributed fluidic elastomer actuators, as well as drive cylinders that supply fluid energy. Next, using this model and trajectory optimization techniques we find locally optimal open-loop policies that allow the system to perform dynamic maneuvers we call *grabs*. In 37 experimental trials with a physical prototype, we successfully perform a grab 92% of the time. Last, we introduce the idea of static bracing for a soft elastomer arm and discuss how forming environmental braces might be an effective manipulation strategy for this class of robots. By studying such an extreme example of a soft robot, we can begin to solve hard problems inhibiting the mainstream use of soft machines.

1 Introduction

Industrial-style manipulators have discrete joints and rigid links. They have been transformative for industrial repetitive tasks. However, these robots are often considered too rigid for human-centered environments where the tasks are unpredictable and the robots have to ensure that their interaction with the environment and with humans is safe. Our goal is to develop soft robot manipulators capable of autonomous, safe, and dynamic interactions with people and their environments. In this paper we present a suite of algorithms for dynamically controlling a soft fluidic elastomer manipulator acting under gravity.

Soft robots are designed with a continuously deformable or continuum body providing the robot with theoretically infinite degrees of freedom; see review by Trivedi et al. [2008]. Soft

robots can conform to variable but sensitive environments exemplified by Chen et al. [2006]. They can adaptively manipulate and grasp novel objects varying in size and shape [McMahon et al., 2006]. And their continuously deformable bodies allows them to squeeze through confined spaces [Shepherd et al., 2011]. Additionally, when robots are made entirely from soft rubber they are extremely resilient to harsh environmental conditions [Tolley et al., 2014b] and can collide harmlessly with their environment [Marchese et al., 2014a]. However, the softer we make robots the less predictable their motions become. Robots made entirely from soft elastomer and powered by fluids do not yet have well understood models nor planning and control algorithms primarily because their intrinsic deformation is continuous and highly compliant. Additionally, such systems are often underactuated; they can contain many passive degrees of freedom (DOF), and when driven with low pressure fluids the available input fluid power is unable to compensate for gravitational loading incurred at appreciable bend angles.

In this work we provide an approach for dynamically controlling soft robots. That is, an entirely soft fluid-powered multi-segment spatial robot can be autonomously positioned to accomplish tasks outside of its gravity compensation envelope. Specifically, we begin by developing a dynamic model for such a soft manipulation system as well as a computational strategy for identifying the model. Then, we use this model and trajectory optimization methods to execute dynamic motion plans. Through simulation and experiments we demonstrate repeatable positioning of the aforementioned manipulator to states outside of the statically reachable workspace in dynamic maneuvers we call *grabs* (See Fig. 1). For example, consider a soft manipulator that can safely and dynamically interact with humans by quickly grabbing objects directly from a human’s hand. Additionally, this type of soft manipulator is well-suited for safely bracing itself against nearby surfaces, the same way we humans rest our wrists against a table while we write. We show that required bracing forces for such a soft manipulator are generally small compared to a rigid bodied manipulator and that braces can generally be accomplished on a wider range of bracing surfaces. To the best of our knowledge, this is the first instance of dynamic motion control for a soft fluidic elastomer robot.

*Andrew D. Marchese, Russ Tedrake, and Daniela Rus are with the Computer Science and Artificial Intelligence Laboratory, Massachusetts Institute of Technology, 32 Vassar St. Cambridge, MA 02139, USA, {andy, russt, rus}@csail.mit.edu

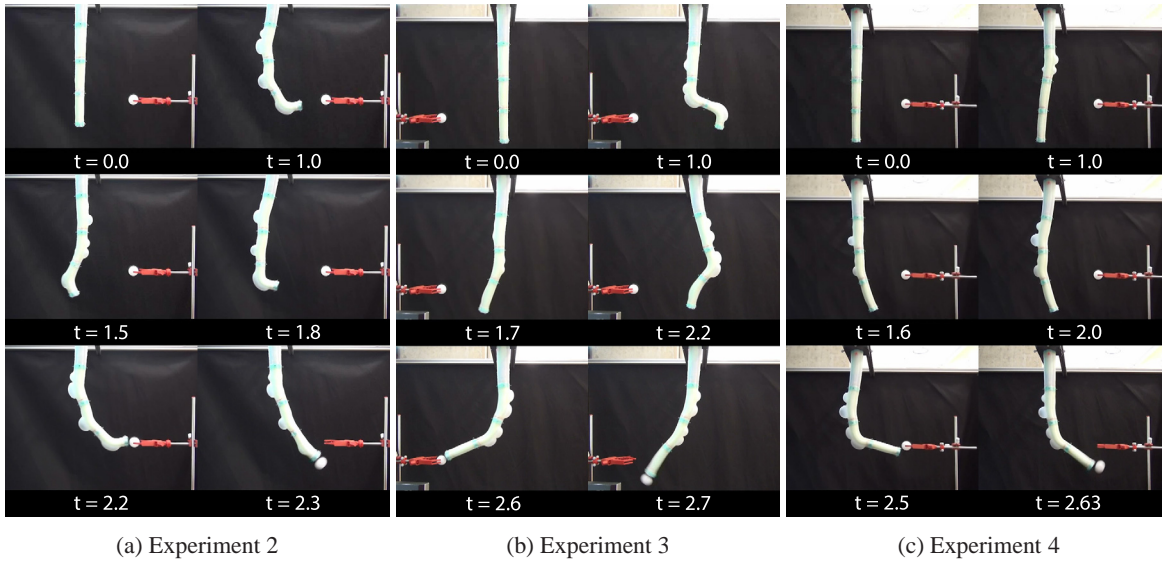


Figure 1: Sequenced photographs from experiments two, three, and four.

1.1 Prior Work

Soft robots have continuously deformable backbones that undergo large deformations. This attribute means soft robots are a subclass of continuum robots, as reviewed by Robinson and Davies [1999]. However, not all continuum robots are *soft* and even continuum robots referred to as *soft* have varying degrees of rigidity.

1.1.1 Dynamics and Control for Continuum Robots

Purely kinematic approaches to continuum robot control and planning work in simulation and when the robot is sufficiently constrained by the rigidity of its actuators or backbone. For example, Hannan and Walker [2003] develop novel continuum kinematics for a hyper-redundant elephant trunk and demonstrate how these enable capabilities like obstacle avoidance. Jones and Walker [2006b] and Jones and Walker [2006a] provide kinematic algorithms for controlling the shape of multi-segment continuum manipulators. Chirikjian and Burdick [1995] use a continuous backbone model to plan optimal hyper-redundant manipulator configurations using calculus of variations. Additionally, Xiao and Vatcha [2010] introduce a planar continuum arm planner that enables simulated grasping in uncertain, cluttered environment.

Dynamic models of continuum robots open the door for a variety of control techniques. Chirikjian [1994] uses a continuum approach to model the dynamics of a hard hyper-redundant manipulator and uses this for computed torque control. Mochiyama and Suzuki [2002] develop a dynamic model of a flexible continuum manipulator based on infinitesimal slices of the arm orthogonal to its backbone. Gravagne and Walker [2002] dynamically model the Clemson Tentacle Manipulator, a hard continuum robot, and show a PD plus feed-forward regulator is sufficient for stabilizing the system. They further develop a large deflection model and controller in Gravagne et al. [2003]. Snyder and Wilson [1990] and Wil-

son and Snyder [1988] dynamically model polymeric pneumatic tubes subject to tip loading using a bending beam model but do not use this for control. Using a Lagrangian approach Tatlicioglu et al. [2007] develop a dynamic model for and provide simulations of a planar extensible continuum manipulator. Braganza et al. [2007] develop a neural network controller for continuum robots such as OctArm [McMahan et al., 2005] based on a dynamic model.

1.1.2 Dynamics and Control for Soft Elastomer Robots

To the best of our knowledge, highly compliant robots whose bodies are made from soft elastomer and distributed fluidic actuators have not used dynamic model-based control. Prior work in this field uses model-free, open-loop control policies, but because this existing work does not derive control policies from nonlinear dynamic models these approaches cannot efficiently plan motions for novel tasks without sufficient *manual* trial-and-error. Most fluid powered soft robots use model-free open-loop valve sequencing to control body segment bending. That is, a control valve is turned on for a user-determined duration of time to pressurize an elastomer actuator and then off to either hold or deflate the actuator. For instance, there are soft rolling robots [Correll et al., 2010, Onal et al., 2011, Marchese et al., 2011] made of fluidic elastomer actuators that use this control approach. A self-contained, autonomous soft-bodied fish developed by Marchese et al. [2014c] uses such a controller to locomote. Also a soft snake-like robot developed by Onal and Rus [2013] uses this open-loop scheme to enable serpentine locomotion. Luo et al. [2014] develop and verify a planar dynamic model for this soft snake but do not use it for control. Again, Shepherd et al. [2011] use a model-free open-loop valve controller to drive body segment bending in an entirely soft multigait robot. Passive control is demonstrated in an explosive, jumping robot in Shepherd et al. [2013] and extended to use a valve controller in Tolley et al. [2014a].

Martinez et al. [2013] develop manually operated elastomer tentacles containing 9 PneuNet actuators embedded within 3 body segments. There is also an example of controlling a soft pneumatic inchworm-like robot using servo-controlled pressure described in Lianzhi et al. [2010].

There are several notable examples of soft fluidic elastomer manipulators. Wakimoto et al. [2009] develop a miniature soft hand composed of fiberless fluidic micro actuators where pressurization and vacuuming is driven by a hand syringe. Cianchetti et al. [2013] present a soft elastomer manipulator module that can bend bidirectionally and elongate using positive pressure actuation as well as stiffen using granular jamming. The module is controlled by regulating pressure and powered by a compressor. Deimel and Brock [2013] demonstrate robust grasping performance with a novel soft elastomer hand without using feedback. In these examples, the research is neither focused on dynamic nor computational control. Previously, we have demonstrated an approach to motion control for planar soft elastomer manipulators using closed-loop kinematic control in Marchese et al. [2014b,a], but again a dynamic model was not used in the control strategy.

Open-loop model-free control is also common for soft elastomer robots that do not use pneumatic actuation. For example, previous work on soft bioinspired octopus-like arms developed by Calisti et al. [2010] demonstrate open-loop capabilities like grasping and locomotion [Laschi et al., 2012, Calisti et al., 2011]. Umedachi et al. [2013] developed a soft crawling robot that uses an open-loop SMA driver to control body bending.

1.2 Contributions

Our work builds on this previous work and aims to enable new capabilities for soft manipulation. Specifically, this paper contributes the following:

- A dynamic model for a fluid powered manipulator made entirely from soft elastomer as well as a process for fitting the model to experimental data;
- Dynamic control algorithms that allow such a soft manipulator operating under gravity to be precisely positioned;
- Manipulation primitives built on these dynamic control algorithms, grabbing and bracing; and
- Extensive experiments with a physical prototype.

This paper significantly extends an original conference publication Marchese et al. [2015b] and is organized as follows: in Section 3 we develop a dynamic model for an entirely soft fluid powered manipulator whose design is detailed in Marchese and Rus [2015]. In Section 4 we describe a process for identifying the manipulator as well as its actuators and drive mechanisms. Section 5 explores *grabbing* as a manipulation primitive. These autonomous dynamic maneuvers enable the soft arm to reach areas that are statically unreachable due to gravity. Similarly, this section provides an overview of the grabbing strategy, an algorithm for planning and executing

grabs, as well as evaluations of this motion primitive in both simulation and with a physical prototype of the aggregate manipulation system. Section 6 discusses the strategy of static bracing as a manipulation primitive. Here, we provide conditions for feasible bracing, an algorithm for planning and executing a simple normal force brace, as well as evaluate this concept in simulation. Finally Section 7 provides a conclusion and discussion of future work.

2 Device Overview

To start, we provide the reader with a brief overview of the soft arm prototype and its drive mechanisms developed by the authors in Marchese and Rus [2015]. The soft arm is pictured in an unactuated configuration in the left panel of Figure 2. It is composed entirely of low durometer rubber and is powered by fluidic elastomer actuators. These actuators are distributed throughout the arm’s four body segments and allow each segment to bend with two actuated degrees of freedom. For more information on fluidic elastomer actuator designs and fabrication techniques also refer to Marchese et al. [2015a]. Driving actuation is an array of fluidic drive cylinders (Fig. 2 right). These devices consist of a fluidic cylinder at (a) coupled to an electric linear actuator at (b). They move fluid into and out of the arm’s soft actuators in a closed circuit and provide continuous adjustment of fluid flow. The actuated region of one of the

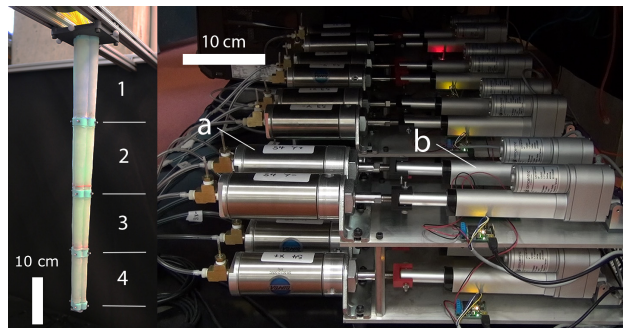


Figure 2: Left: A soft continuum manipulator composed entirely from low durometer rubber developed by the authors in Marchese and Rus [2015]. The manipulator has four independently actuatable body segments, each capable of 2 degree of freedom bending. In this work, an external camera system is used to localize soft connectors between arm segments shown in green. Right: An array of high capacity fluidic drive cylinders [Marchese et al., 2014b] used to drive the manipulator’s distributed fluidic elastomer actuators. Each drive mechanism consists of a pneumatic cylinder (a) driven by an electric linear actuator (b). The primary benefits of this drive mechanism are that it is closed circuit and allows realization of continuously variable flow profiles.

manipulator’s soft arm segments is observed to bend with approximately constant curvature κ and bend angle θ (i.e. $\kappa = \frac{\theta}{L}$) within a sagittal plane defined by the bend angle orientation γ . In order to transform from a segment’s base to a point s along the neutral axis of its actuated region, i.e. $s = [0, L]$ where L

is undeformed actuator length, we use the following kinematic model transformation

$$\mathbf{S}_s^{base} = \mathbf{R}_z(\gamma) \mathbf{T}_z(L_P) \mathbf{R}_y\left(\frac{\kappa s}{2}\right) \mathbf{T}_z(d(\kappa s)) \mathbf{R}_y\left(\frac{\kappa s}{2}\right), \quad (1)$$

where \mathbf{R} and \mathbf{T} are rotations and translations about and along the subscript axes, and L_P is the length of the segment's unactuated region and accounts for deadspace produced by channel inlets and/or soft end-plate connectors. This model is consistent with continuum manipulator literature [Webster and Jones, 2010] and is developed and validated in the context of the soft fluidic elastomer manipulator in Marchese and Rus [2015].

The transformation from base to tip of a multi-segment soft arm composed of N segments confined to a sagittal plane defined by γ can be represented by cascading single segment transformations together

$$\mathbf{M}_{tip_N}^{base} = \mathbf{S}_{tip}^{base}(\gamma, \theta_1) \mathbf{S}_{tip}^{base}(0, \theta_2) \cdots \mathbf{S}_{tip}^{base}(0, \theta_N). \quad (2)$$

3 Dynamic Model

To begin, we develop a dynamic model. The benefit of using a dynamic model within the iterative learning control algorithm is that control policies can be generated using a model-based open-loop policy search algorithm, such as trajectory optimization, and these are well-suited for underactuated systems.

3.1 Energetics

Our objective is to write the equations of motion for this soft fluidic elastomer manipulator. To do this we can first find the potential, kinetic, and input components of energy for a single arm segment and then use a Lagrangian approach to derive the equations of motion with respect to the segment's generalized coordinate. A fundamental difference between soft and hard robot manipulators is in the way energy is stored. In a soft fluidic elastomer manipulator, input fluid energy is delivered from a power supply and stored as both strain energy along its continuum segments V_ϵ and gravitational potential energy V_g . Both forms of stored energy serve to deform the manipulator and are transferred to kinetic energy T . However, it is important to note that just as in a more traditional robotic system, not all of the supplied fluidic energy is stored in the robot and this is primarily due to losses in the transmission system. The complete energy description is

$$\int_0^{\mathbb{V}_o} p_s(\mathbb{V}) d\mathbb{V} = V_\epsilon + V_g + V_f + T_r + T. \quad (3)$$

Here, the left hand side represents the total energy output by a fluidic power supply. The volume output by the supply is \mathbb{V}_o and this volume is a function of time, i.e. $\mathbb{V}(t) = \int_0^t v(t) dt$ where v is fluid flow. The supply's pressure p_s is a function of volume. The right hand side describes how this energy is

expended in the aggregate manipulation system. Due to the relative compressibility of the transmission fluid, a component of output energy V_f is stored in the residual volume of the fluid supply and transmission line and never makes it to the manipulator. Additionally, a component of delivered energy T_r is lost due to the resistivity of the fluid transmission line and viscous fluid friction. This component of energy generally increases as soft actuators are driven at higher actuation rates [Marchese et al., 2014c].

3.1.1 Potential Energy of a Segment

Consider a single arm segment deforming in a sagittal plane defined by a fixed γ . By approximating the center of mass to be located half-way along the segment's neutral axis, we can use \mathbf{S}_s^{base} to express the center of mass position in \mathbb{R}^3 as $(x_m(\theta), y_m(\theta), z_m(\theta))$. Bend angle θ is understood to be time dependent. The gravitational potential energy of the segment is

$$V_g(\theta) = m g z_m(\theta) \quad (4)$$

where m is the segment's mass and g is the gravitational constant. For a fluidic soft manipulator made of deformable elastomer, a significant component of potential energy is strain energy. For strain below 60%, we can approximate the stress strain relationship of the arm segment's outer layer with a constant elastic modulus E . This was determined from the specific material properties of the chosen elastomer. With this, the strain energy developed in an actuated channel is

$$V_\epsilon = \frac{1}{2} \vee E \epsilon^2 \rightarrow V_\epsilon = \frac{1}{2} \pi \bar{t} (\bar{h} + \bar{t}) L E \epsilon^2 \quad (5)$$

where ϵ is material strain, \vee is the material volume incurring strain, and \bar{t} and \bar{h} are the wall thickness and diameter of the actuated channel. In a segment subject to circumferential and longitudinal strain that deforms under constant curvature, material strain ϵ and bend angle θ can be related by decomposing the actuated region into J cross-sectional x-y slices of z-axis length w as outlined in Marchese and Rus [2015] and the law of cosines

$$\epsilon_j = \frac{\bar{h}_j}{w_j} \sqrt{2 - 2 \cos \theta_j} \quad \forall j = 0..J \rightarrow \epsilon = \frac{\bar{h}}{w} \theta. \quad (6)$$

There are several important observations that allow us to express this relationship between ϵ and θ : First, the dimensions of each slice are uniform under the aforementioned constant curvature assumption. Second, in general \bar{h} is not constant, but rather changes as a function of strain $\bar{h}(\epsilon)$ and this is consistent with the analysis contained in Shepherd et al. [2011] where pneumatic channels similar to the type described here increase in stiffness and potential energy when pressurized. However, we observe that after undergoing initial circumferential expansion, the diameter of the actuated channels here changes little. Approximating the diameter \bar{h} to be constant is valid to describe the regime of operation after the initial circumferential change. Lastly, using the small angle approximation $\cos \theta \approx 1 - \frac{\theta^2}{2}$ for the argument $\frac{\theta}{J}$ where J is chosen such

that the approximation is valid, we can linearize the relationship between ϵ and θ in order to arrive at a constant stiffness coefficient and help reduce the complexity of the model.

Now, we can write strain energy in the segment as a function of bend angle

$$V_\epsilon(\theta) = \frac{1}{2} \left(\frac{\pi \bar{t} (\bar{h} + \bar{t}) L E \bar{h}^2}{w^2} \right) \theta^2 \rightarrow V_\epsilon(\theta) = \frac{1}{2} k \theta^2, \quad (7)$$

where k is an effective stiffness for the generalized coordinate θ . The total potential energy of the arm segment in the sagittal plane defined by γ is $V(\theta) = V_g + V_\epsilon$.

3.1.2 Kinetic Energy of a Segment

The total kinetic energy T of a soft segment within the sagittal plane as a function of the generalized coordinate is

$$T(\theta) = \frac{1}{2} m \left(\frac{\partial x_m}{\partial t} + \frac{\partial z_m}{\partial t} \right)^2 \quad (8)$$

3.1.3 Input to a Segment

We develop an independent generalized force τ that acts on an arm segment by differentiating the total potential energy with respect to the generalized coordinate, i.e. $\tau = \frac{\partial}{\partial \theta} V$

$$\tau = k \theta + a g L m \cos\left(\frac{\theta}{2}\right) \theta - \frac{1}{4} g L m \sin\left(\frac{\theta}{2}\right) (-1 + a \theta^2) \quad (9)$$

We can substitute in the approximations $\sin\left(\frac{\theta}{2}\right) \approx \theta$ and $\cos\left(\frac{\theta}{2}\right) \approx 1 - \frac{1}{8}\theta^2$ with less than 5% error at θ equal to 50° and 100° respectively

$$\tau = k \theta + \frac{1}{8} (1 + 8a) g L m \theta - \frac{1}{4} a g L m \theta^3. \quad (10)$$

This approximation will help simplify the identification process in Section 4.3. Next, we can express the change in channel volume \mathbb{V}_c as a function of material strain and, because of our aforementioned strain assumption, a function of θ

$$\mathbb{V}_c = \frac{1}{2} \frac{\pi \bar{h}^2}{4} L \epsilon \rightarrow \mathbb{V}_c = \frac{\pi \bar{h}^3 L}{8 w} \theta. \quad (11)$$

Substituting this into the generalized force yields:

$$\tau = -\frac{128 a g m w^3}{L^2 \pi^3 \bar{h}^9} \mathbb{V}_c^3 + \left(\frac{8 k w}{\pi \bar{h}^3 L} + \frac{(1 + 8a) g m w}{\pi \bar{h}^3} \right) \mathbb{V}_c, \quad (12)$$

revealing that there is a cubic relationship between the generalized force and the change in channel volume.

3.2 Multi-Segment Equations of Motion

We can write the equations of motion for a multi-segment soft manipulator using multiple generalized coordinates as follows. The center of mass position of the n^{th} soft segment is represented by \mathbf{P}_n and can be expressed as

$$\mathbf{P}_n = M_{tip_{n-1}}^{base} S_{\frac{L_n}{2}}^{base} \mathbf{0} \quad \forall n = 1 \dots N, \quad (13)$$

where $\mathbf{0}$ is a vector of zeros. The total kinetic energy of a manipulator with N segments is

$$T = \sum_{n=1}^N \frac{1}{2} m_n \frac{d}{dt} \mathbf{P}_n \cdot \frac{d}{dt} \mathbf{P}_n. \quad (14)$$

And the total potential energy is

$$V = \sum_{n=1}^N \frac{1}{2} k_n \theta_n^2 + g \sum_{n=1}^N m_n \mathbf{P}_n \cdot \hat{\mathbf{k}}. \quad (15)$$

Using the Lagrangian $L = T - V$, N independent nonlinear equations of motion can be written, one for each generalized coordinate

$$\frac{d}{dt} \frac{\partial L}{\partial \dot{\theta}_n} - \frac{\partial L}{\partial \theta_n} = \tau_n - b_n \dot{\theta}_n \quad \forall n = 1 \dots N. \quad (16)$$

where b is a damping term used to account for the non-conservative nature of the generalized forces. The soft robot dynamics can now be written in traditional manipulator equation form

$$\mathbf{H}(\theta) \ddot{\theta} + \mathbf{C}(\theta, \dot{\theta}) \dot{\theta} + \mathbf{G}(\theta) = \mathbf{B} \tau. \quad (17)$$

Figure 3 provides an illustration of this model for a soft manipulator composed of four segments. The sagittal plane is defined by a traditional rotational degree of freedom γ located at the manipulator's base. In the most general case, the dynamic model is parameterized by four generalized coordinates $\theta_1 \dots \theta_4$ and four corresponding segment masses \mathbf{m} , generalized stiffnesses \mathbf{k} , and damping coefficients \mathbf{b} . Additionally there are three generalized input forces τ .

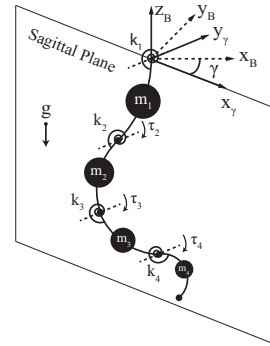


Figure 3: Visualization of the multi-segment soft manipulator model. The base frame is rotated by γ by a traditional rotational degree of freedom and defines the sagittal plane within which the manipulator moves. The first soft segment is unactuated.

4 System Identification

In order to use the dynamic model developed in Section 3 for automated control we must first develop a strategy for identifying the model's unknown physical parameters. In addition

to this, we must also define an approach for identifying an accurate model for the manipulator's soft actuators as well as its drive mechanisms. In this section we first present a high-level algorithm used to identify the aggregate manipulation system composed of three distinct subsystems: fluidic drive cylinders, distributed soft actuators, and the soft manipulator. Then, we look specifically at how these unknown model parameters arise from each subsystem.

4.1 Approach Overview

Identification of the aggregate dynamical manipulation system arm is performed by iteratively adjusting a parameter set \mathbf{p} such that a model instantiated from \mathbf{p} follows the same N -segment endpoint Cartesian trajectory as measured on the physical system. Specifically, we do this by solving the nonlinear optimization within Algorithm 1 for a locally optimal parameter set \mathbf{p}^* . Here, $\mathbf{E}_{n,i}$ is a discrete trajectory of the

Algorithm 1: System Identification

$$\begin{aligned} \min_{\mathbf{p}} \quad & \sum_i \sum_{n=1}^N \|arm.FORWARDKIN_n(\mathbf{x}_i) - \mathbf{E}_{n,i}\| \\ \text{subject to} \quad & arm \leftarrow \text{UPDATEMODEL}(\mathbf{p}) \\ & \mathbf{x}(t) \leftarrow \text{SIMULATE}(\mathbf{u}(t), arm, [0, t_f], \mathbf{x}_0), \\ & i = \lfloor \frac{t}{dt} \rfloor \quad \forall t = 0 \dots t_f. \end{aligned}$$

And initial conditions \mathbf{x}_0 are found according to

$$\begin{aligned} \mathbf{x}_0 = \min_{\mathbf{x}} \quad & \sum_{n=1}^N \|arm.FORWARDKIN_n(\mathbf{x}) - \mathbf{E}_{n,0}\| \\ \text{subject to} \quad & x_n^{min} \leq x_n \leq x_n^{max} \quad \forall n = 1 \dots N. \end{aligned}$$

measured cartesian endpoint coordinates of the n^{th} arm segment. The manipulator state trajectory $\mathbf{x}(t)$ is composed of segment bend angles $\boldsymbol{\theta}$ and corresponding velocities $\dot{\boldsymbol{\theta}}$. The function FORWARDKIN_n uses the multi-segment transformation to return the cartesian endpoint coordinates of the n^{th} arm segment. The function UPDATEMODEL instantiates arm according to the parameter set \mathbf{p} and the function SIMULATE forward simulates the response of the dynamic model to input trajectory $\mathbf{u}(t)$ over the time interval $t = [0, t_f]$ from initial conditions \mathbf{x}_0 .

The aggregate manipulation system arm consists of four fluidic drive cylinder pairs (Figure 2 right panel) connected to eight fluidic elastomer actuators distributed within the soft manipulator. We break this aggregate system into three distinct subsystems with the following input \rightarrow output relationships:

1. Fluidic Drive Cylinders:
reference inputs $\mathbf{u} \rightarrow$ cylinder displacements \mathbb{V}_s
2. Fluidic Elastomer Actuators:
cylinder displacements $\mathbb{V}_s \rightarrow$ generalized torques $\boldsymbol{\tau}$
3. Soft Manipulator:
generalized torques $\boldsymbol{\tau} \rightarrow$ manipulator states \mathbf{x}

Both the dynamic manipulator model and system identification algorithm were implemented using Drake [Tedrake, 2014], which is an open-source planning, control, and analysis toolbox for nonlinear dynamical systems.

4.2 Fluidic Drive Cylinders

Volumetric fluid changes to each agonistic pair of embedded channels within a soft arm segment are controlled by a pair of position-controlled fluidic drive cylinders, a device developed by the authors in Marchese et al. [2014b]. In this work we further develop and identify the device's dynamic model. Each pair is identified as an independent subsystem, and under the sagittal plane assumption N of these subsystems are required.

The input to each subsystem is u , a reference differential volumetric displacement to the position controlled cylinder pair and the output of each subsystem is \mathbb{V}_s , the differential volumetric displacement of the cylinders. One of two identical cylinders in the pair is driven at a time and pressurizes either half of the attached bending segment.

To experimentally identify this subsystem we conduct several trials of the same experiment. The experiment consists of exciting the system with a reference wave $u(t)$ that is the summation of W sinusoidal waves with randomized phase delays ϕ , frequencies ω , and amplitudes a_w randomly sampled from a Bretschneider wave spectrum $S^+(\omega)$ with peak frequency ω_p of 2π and significant wave height ζ equal to twice the maximum displacement \mathbb{V}_{max} .

$$u(t) = \sum_{i=1}^W a_{w_i} \sin(\omega_i t + \phi_i), \quad (18)$$

$$S^+(\omega) = \frac{1.25}{4} \frac{\omega_p^4}{\omega^5} \zeta^2 \exp\left(-1.25 \left(\frac{\omega_p}{\omega}\right)^4\right). \quad (19)$$

We fit a second order state space model to measured input-output data from one of five trials and then validated the model prediction against the remaining four trials. An example verification is shown in Figure 4. The identification and verification process was repeated for each of the 4 cylinder pairs used in later experiments.

4.3 Fluidic Elastomer Actuators

To identify the dynamics of the arm's soft actuators, we rely on the predicted cubic relationship between internal channel volume \mathbb{V}_c and generalized torque τ as developed in Section 3.1.3. Also, the relationship between piston pressure p_s and channel volume \mathbb{V}_c indicates a delay due to the impedance of the fluid transmission line. Combining these effects, we define a simplified identifiable model in the form

$$\tau(t) = c \mathbb{V}_s^3(t - t_d). \quad (20)$$

The model constants \mathbf{c} for each actuator pair and a single t_d are added to the main algorithm's parameter set \mathbf{p} for identification, as the soft actuators are subject to dynamic fatigue and their performance is susceptible to change over time.

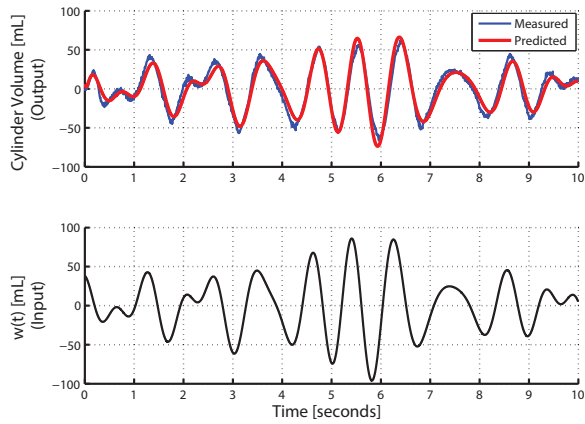


Figure 4: Example experimental identification of a position controlled fluidic drive cylinder subsystem. The identification process consists of exciting each independent subsystem with several randomized wave profiles and fitting and verifying a two state LTI black-box model to measured input-output data. Top: model predicted and measured output in blue and red respectively. Bottom: subsystem input.

To validate this input output relationship, we again perform several trials of the aforementioned experiment, this time deriving actuator torque through a custom apparatus that measures the blocked tip force exerted by a segment fixed at its base. Figure 5 shows an example input-output identification for this subsystem.

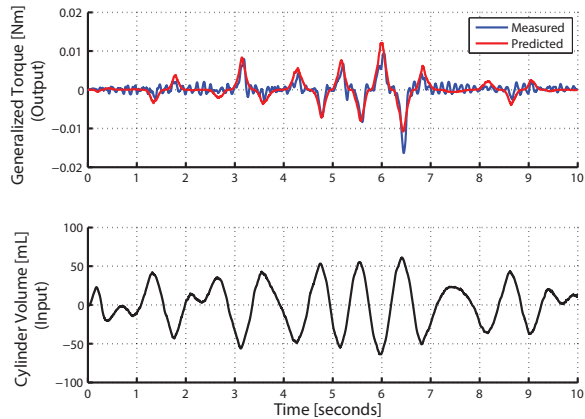


Figure 5: Example experimental identification of a soft actuator subsystem. Again the identification process consists of exciting each independent subsystem with several randomized wave profiles, but here we fit and verify a two parameter non-linear model to measured input-output data. Top: model predicted and measured output in blue and red respectively. Bottom: subsystem input.

4.4 Soft Manipulator

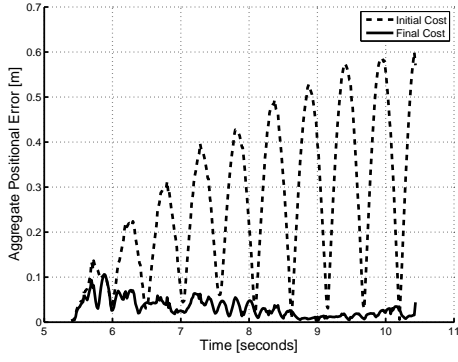
The manipulator's dynamic model is symbolically parameterized by N masses \mathbf{m} , stiffnesses \mathbf{k} , and damping coefficients \mathbf{b} . In the actuated case, there are also N additional actuator

parameters, $N - 1$ unknown coefficients \mathbf{c} and a single time delay t_d . To reduce the parameter set \mathbf{p} from $4N$ parameters to $2N + 2$ parameters we make the following observations: according to the expression for V_ϵ in Section 3.1.1 stiffness changes linearly with channel length L and therefore we can replace \mathbf{k} with $\frac{L_i}{L_1} k$ where i is the segment index and k is a single unknown stiffness. Furthermore, we hypothesize the non-conservative components of force $\mathbf{b} \dot{\theta}$ are similar along the length of the arm, therefore we approximate the coefficients b_i to be equal $\forall i$.

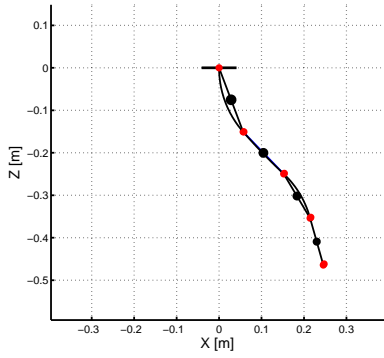
Measurements provided a coarse estimate of each parameter in \mathbf{p} . The identification algorithm, Algorithm 1, then freely adjusts these parameters. Initial mass and stiffness parameters were bound by a $\pm 38\%$ and $\pm 23\%$ change respectively, and the damping coefficient was adjusted on the interval $[1, 5] \cdot 10^{-3}$. Multiple identifications were performed using random perturbations in the initial parameter set. Table 1 summarizes the results 4 trials and Figure 6a shows an example initial and final aggregate positional error between measured and simulated segment endpoints over time. When summed over time this is the algorithm's objective function.

Table 1: Identification of Passive Arm

	p						cost
	m_1	m_2	m_3	m_4	k	b	$\sum_i \sum_n$
			(kg)		(N m)	(N m s)	(m)
Initial	0.21	0.17	0.085	0.065	0.12	$2.0 \cdot 10^{-3}$	10
Final	0.190	0.146	0.090	0.090	0.108	$4.2 \cdot 10^{-3}$	0.969
	± 0.012	± 0.001	± 0.002	± 0.003	± 0.003	$\pm 0.1 \cdot 10^{-3}$	± 0.004



(a)



(b)

Figure 6: At (a) the positional error between measured and simulated endpoints summed over segments both for the initial parameter set (dashed line) and final parameter set (solid line) over time. At (b) the initial pose of the arm is shown at $\dot{\theta} = 0$. Measured segment endpoints are shown in red and the modeled neutral axis of the arm is shown in black. The black circles indicate the approximated center of mass locations.

5 Grabbing

5.1 Grabbing Overview

A primitive enabled by the developments in Sections 3 and 4 is grabbing. Grabbing is defined as bringing the arm's end effector to a user specified, statically unreachable goal point with near zero tip velocity. Grabbing is an advantageous strategy to employ during manipulation as it enables the soft arm to reach areas that are statically unreachable due to gravity.

There are several major challenges that arise when trying to autonomously move the soft manipulator. First, we leave the top segment unactuated to accommodate external loads acting on the distal segments. Second, the system is tightly constrained by generalized torque limits. That is, the low operating pressures of the fluidic actuators in combination with their very low durometer rubber composition equate to constraints on input forces. To exemplify this problem consider the following search for feasible solutions that statically position the arm's end effector to a goal point in task space

$$\begin{aligned}
 &\text{find} \quad \text{s.t.} \quad \mathbf{C} - \mathbf{B}\boldsymbol{\tau} = \mathbf{0}, \\
 &\boldsymbol{\tau}, \boldsymbol{\theta} \quad \|\text{arm.FORWARDKIN}_N(\boldsymbol{\theta}) - \text{Goal}\| - \epsilon = 0, \\
 &\quad \tau_m^{\min} \leq \tau_m \leq \tau_m^{\max} \quad \forall m = 1 \dots M, \\
 &\quad \theta_n^{\min} \leq \theta_n \leq \theta_n^{\max} \quad \text{and} \quad \dot{\theta}_n = 0 \quad \forall n = 1 \dots N.
 \end{aligned} \tag{21}$$

By looking for solutions to goal points in the vicinity of the end effector, we quickly bring to light the limitations of a purely kinematic approach to motion planning for this class of manipulators subject to gravity. Figure 7 depicts feasible static solutions in green for identified arms under estimated torque limits.

5.2 Grabbing Algorithms

We develop an algorithm, Algorithm 2, that can plan and execute a grab maneuver. The algorithm uses trajectory optimization to both plan a locally-optimal policy in generalized torque space as well as to determine an optimal input trajectory to the aggregate manipulation system to realize this policy. The trajectory optimizations were implemented using Drake Tedrake [2014]. Algorithm 2 can be interpreted as an iterative learning control, which after a couple grabbing attempts is able to successfully perform the desired maneuver.

Algorithm 2: Iterative Learning Control

```

 $arm_0 \leftarrow \text{SYSTEMID}(\mathbf{x}_m(t), \mathbf{u}(t)).$ 
 $i = 0.$ 
while Goal is not met do
     $\boldsymbol{\Pi} \leftarrow \text{TRAJOPT}(arm_i, \text{Goal}).$ 
     $\mathbf{u}(t) \leftarrow \text{INVERTACTUATORS}(arm_i, \boldsymbol{\Pi}).$ 
     $\mathbf{x}_m(t) \leftarrow \text{RUNPOLICY}(\mathbf{u}(t)).$ 
     $arm_{i+1} \leftarrow \text{SYSTEMID}(arm_i, \mathbf{x}_m(t), \mathbf{u}(t)).$ 
     $i++.$ 
end

```

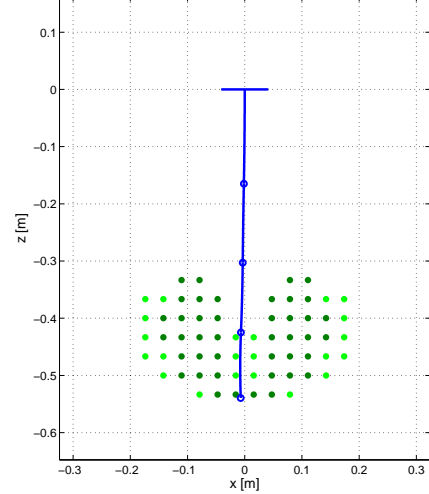


Figure 7: Feasible static solutions for an identified soft manipulator under estimated torque limits. The solid blue lines represent the initial state of the manipulator. Dark and light green circles indicate points that were statically reachable under the torque limits of $|\boldsymbol{\tau}| = [0.13, 0.13, 0.13, 0.13]^T$ and $|\boldsymbol{\tau}| = [0, 0.12, 0.13, 0.18]^T$ respectively.

Here, $\mathbf{x}_m(t)$ represents a measured state trajectory of the soft manipulator over the time interval $t = [0, t_f]$, $\mathbf{u}(t)$ is the reference input trajectory to the manipulation system, and $\boldsymbol{\Pi}$ represents a matrix of locally-optimal generalized torque and state trajectories. The function SYSTEMID describes the identification process in Section 4, the functions TRAJOPT and INVERTACTUATORS embody processes described in Subsections 5.2.1 and 5.2.2, and RUNPOLICY represents executing the reference input policy $\mathbf{u}(t)$ on the physical manipulation system.

5.2.1 Trajectory Optimization

We use a direct collocation approach to trajectory optimization von Stryk [1993] in line 4 of Algorithm 2. In short, this is a model-based open-loop policy search that finds a feasible input trajectory that moves the manipulator from an initial state to a goal state given both input and state constraints. The policy $\boldsymbol{\Pi}$ can generally be a function of both state and time, but in this case is parameterized by $M \times \frac{t_f}{dt}$ free parameters α where M is the number of inputs and dt is a discrete time step

$$\boldsymbol{\Pi}_\alpha(\mathbf{x}, t) = \alpha_{m,i} \quad \forall m = 1 \dots M, \tag{22}$$

$$i = \lfloor \frac{t}{dt} \rfloor \quad \forall t = 0 \dots t_f. \tag{23}$$

In the case of the soft manipulator each α is a generalized torque τ for each actuated segment augmented with the manipulator's state vector at each time step

$$\boldsymbol{\Pi}_\alpha = \begin{bmatrix} \tau_0 & \tau_1 & \tau_2 & \dots & \tau_{\frac{t_f}{dt}} \\ \mathbf{x}_0 & \mathbf{x}_1 & \mathbf{x}_2 & \dots & \mathbf{x}_{\frac{t_f}{dt}} \end{bmatrix}. \tag{24}$$

The following trajectory optimization is performed to identify a locally-optimal policy Π_α^*

$$\begin{aligned}
\Pi_\alpha^* &= \min_\alpha \sum_i g(\mathbf{x}_i, \tau_i) \quad \Leftarrow \text{Objective Function} \\
\text{subject to} \quad & 0 = \mathbf{x}_i - f(\mathbf{x}_{i-1}, \tau_{i-1}) \, dt - \mathbf{x}_0 \quad \forall i = 1 \dots \frac{t_f}{dt}, \\
& 0 = h(\mathbf{x}_{t_f}), \quad \Leftarrow \text{Enforce Tip Motion} \\
& \tau_m^{\min} \leq \tau_{m,i} \leq \tau_m^{\max} \quad \text{and} \quad \tau_{m,0} = 0 \quad \forall m, \forall i, \\
& \theta_n^{\min} \leq \theta_{n,i} \leq \theta_n^{\max} \quad \forall n, \forall i, \\
& \theta_{n,0} \leftarrow \text{measured} \quad \text{and} \quad \dot{\theta}_{n,0} = 0 \quad \forall n.
\end{aligned} \tag{25}$$

The first line of constraints forces the policy to obey the manipulator's dynamics and leverages a sequential quadratic program's ability to handle constraints. The second line consists of general nonlinear constraints enforced at the last point in the trajectory $t = t_f$. In the specific case of performing a *grab* we formulate h as follows:

$$h_p = \|\text{arm.FORWARDKIN}_N(\boldsymbol{\theta}) - \text{Goal}\| - \varepsilon_p, \tag{26}$$

$$h_v = \|\text{arm.FORWARDVEL}_N(\boldsymbol{\theta}, \dot{\boldsymbol{\theta}})\| - \varepsilon_v, \tag{27}$$

where h_p constrains end effector position to the goal point and h_v constrains end effector velocity to be near zero at the point in time the goal is reached. In both constraints ε represents a definable error tolerance.

For the task of grabbing, the objective function $g()$ can be used to minimize end effector velocity at t_f , i.e. taking the form $g(\mathbf{x}_{t_f}) = \|\text{arm.FORWARDVEL}_N(\mathbf{x}_{t_f})\|$. Alternatively, $g()$ can be used to find a minimal effort policy and take the form $g(\tau_i) = \tau_i^T R \tau_i$, where R is a scalar weight.

5.2.2 Inverting Actuators

The manipulator's motion is planned in reference to its generalized torques. Using the soft actuator model developed in Section 4.3, this motion plan can be expressed in reference to cylinder displacements \mathbb{V}_s^m , where superscript m denotes an individual cylinder model for each input

$$\mathbb{V}_s^m(t) = \begin{cases} -1^{2/3} \frac{\tau_m^{1/3}(t)}{a_m^{1/3}} & : \tau_m(t) \leq 0 \\ \frac{\tau_m^{1/3}(t)}{a_m^{1/3}} & : \tau_m(t) > 0 \end{cases} \tag{28}$$

Since the target motion plan $\mathbb{V}_s^*(t)$ is a volume profile, many alternative drive systems can be used to realize the manipulator's trajectory, e.g. high pressure gas and valves Marchese et al. [2014c], rotary pumps Onal and Rus [2013]Katzschmann et al. [2014], or fluidic drive cylinders Marchese et al. [2014b]Marchese et al. [2014a]. In this work we use fluidic drive cylinders and this approach allows us to closely match the prescribed volume profile. To effectively invert the LTI fluidic drive cylinder model, developed in the Section 4.2, we use M direct collocation trajectory optimizations. In these prob-

lems

$$\Pi_\alpha^m = \begin{bmatrix} u_0^m & u_1^m & u_2^m & \dots & u_{t_f/dt}^m \\ x_0^m & x_1^m & x_2^m & \dots & x_{t_f/dt}^m \end{bmatrix}. \tag{29}$$

And the following optimization, performed for each cylinder model, identifies a locally-optimal reference input $\mathbf{u}^*(t)$. The superscript m has been omitted for convenience

$$\begin{aligned}
\Pi_\alpha^* &= \min_\alpha \sum_i \|\mathbb{V}_s(i) - \mathbf{C} \mathbf{x}_i + \mathbf{D} u_i\| \quad \Leftarrow \text{Track } \mathbb{V} \text{ Profile} \\
\text{subject to} \quad & 0 = \mathbf{x}_i - (\mathbf{A} \mathbf{x}_{i-1} + \mathbf{B} u_{i-1}) \, dt - \mathbf{x}_0 \quad \forall i = 1 \dots \frac{t_f}{dt}, \\
& u^{\min} \leq u_i \leq u^{\max} \quad \forall i \quad \text{and} \quad \mathbf{x}_0 = 0.
\end{aligned} \tag{30}$$

It is important to note that the locally-optimal input trajectories $\mathbf{u}^*(t)$ returned by the above optimization represent the best realization of a given volume profile subject to the dynamic limitations of the drive mechanism. For example, areas of high-frequency oscillation within $\tau^*(t)$ can result in significant localized tracking errors. As a solution, if the discrepancy between simulated model output and volume profile, i.e. $\|\mathbb{V}_s(t) - \mathbf{C} \mathbf{x}(t) + \mathbf{D} \mathbf{u}(t)\|$, exceeds an experimentally determined threshold for some span of time, we simply rerun the policy search procedure with a randomized $\tau(t)$ until a suitable realization is found. Alternative solutions may include planning directly in \mathbf{u} space; however, this requires a single optimization to handle a dynamic model of the entire manipulation system, i.e. manipulator, actuator models, and cylinder models.

5.3 Grabbing Evaluations

5.3.1 Simulations

To validate this approach to dynamic motion planning for the soft arm, we run direct collocation trajectory optimization on an experimentally identified model of the arm. We find a minimal tip velocity open-loop policy that executes a *grab*. Figure 8 depicts four different grab states (A-D) and Figure 9a-9d shows corresponding locally optimal policies generated by the planning approach. Table 2 lists the goal points and corresponding positional errors, or the error between the manipulator's simulated end effector position at t_f and the goal point, as well as simulated end effector velocity at t_f for seven trials per goal point. Positional errors and velocities that exceed ε_p and ε_v are explained by the fact that the trajectory optimization only enforces dynamic constraints every dt , initialized at 80 ms, which is orders of magnitude greater than the time step used to integrate the manipulator's equations of motion in the approximately continuous time simulation.

5.3.2 Experiments

In order to experimentally validate the outlined approach for grabbing with a soft and highly-compliant arm, we conduct multiple trials of four experiments, summarized in Table 3 and

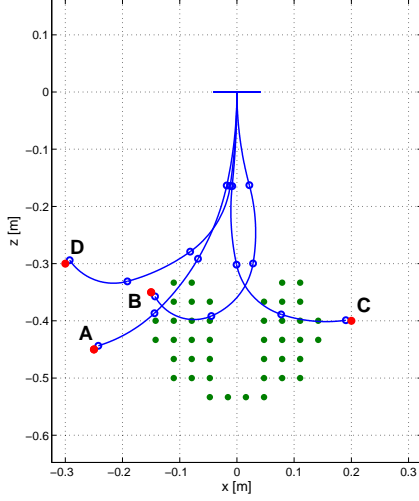


Figure 8: The neutral axis of an experimentally identified model of a four segment soft manipulator is shown in blue at four different grab states (A-D), where the goal position of the grab is shown in red. Green points represent goal positions that are statically feasible under the estimated torque limits of $|\tau| = [0, 0.12, 0.13, 0.18]^T$.

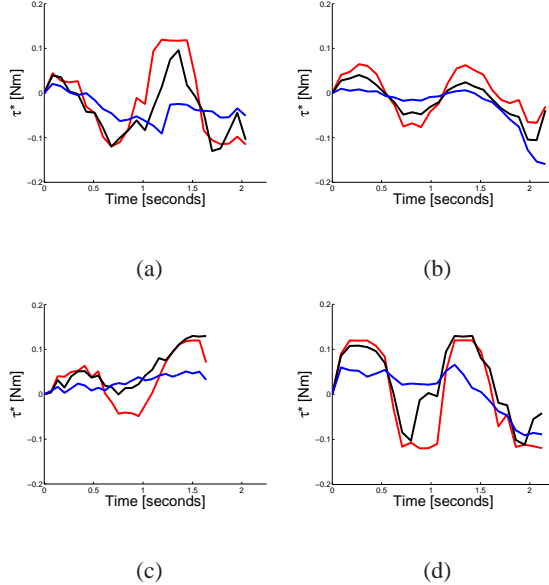


Figure 9: The corresponding locally optimal generalized torque trajectories (a-d) for each of the grab states shown in Figure 8 (A-D), respectively. The input trajectory to segment 2 is shown in red, segment 3 in black, and segment 4 in blue.

Table 2: Dynamic motion planning with direct collocation

Goal	Coordinates (cm)	$R = 0.1$		$R = 0.01$	
		Error (cm)	Velocity (cm·s ⁻¹)	Error (cm)	Velocity (cm·s ⁻¹)
A	(-25, -45)	1.1	1.4	1.1 ± 0.2	1.5 ± 1.2
B	(15, -35)	1.1	2.4	0.8 ± 0.4	2.7 ± 1.0
C	(20, -40)	0.9	0.1	1.0 ± 0.1	0.8 ± 0.4
D	(-30, -30)	1.7*	7.6*	0.9	3.7

$\epsilon_P = 1$ cm and $\epsilon_V = 2$ cm·s⁻¹ in all cases.

*Solver terminated after numerical difficulties.

shown within the video in Extension 1. The goal of these experiments is to have the aggregate manipulation system autonomously perform a grab maneuver. A successful grab is defined as attaching to and removing a 4 cm diameter table tennis ball from a holder at the goal position; refer to Figure 1. Locally-optimal input trajectories $\mathbf{u}^*(t)$, as determined in Section 5.2.2, are executed on the aggregate manipulation system. Trials reported in Table 3 and Figure 10 occurred after successful completion of Algorithm 2. The arm's torque limits are controlled and varied between experiments, i.e. experiments one and two to three and four. Among these groups goal location is also controlled for and varied, i.e. one to two and three to four. In experiments one and two the ball, represented as the black circle in Table 3, is fixed at the user specified goal location around which the plan is derived. In experiments three and four the ball location underwent an initial one-time, experimentally determined adjustment by 2 cm to ensure it corresponded to the simulated realization of the plan, which considers the dynamic limitations of the fluidic drive system. Important simplifications: In these evaluations the unactuated regions between segments \mathbf{L}_p were assumed zero. Additionally, for model stability purposes, the center of mass locations were redefined as

$$\mathbf{P}_n = M_{tip_{n-1}}^{base} \mathbf{R}_z(\gamma) \mathbf{T}_z(L_P) \mathbf{R}_y\left(\frac{\kappa s}{2}\right) \mathbf{T}_z\left(\frac{d(\kappa s)}{2}\right) \mathbf{0} \quad \forall n. \quad (31)$$

This adjustment effectively amplifies center of mass motion as segment curvature increases; However, for segment curvatures achieved during these experiments, this model assumption captures the dynamics of interest.

The aggregate system was able to successfully grab the ball in approximately 92% of trials. Experiments one and two were performed consecutively. Although 2 iterations of system identification were performed on the actuator model parameter set during experiment one, no additional identifications were performed during experiment two. Similarly, experiments three and four were performed consecutively and two identifications were required during experiment three and one during experiment four. Figure 10 shows the cartesian state trajectories of the manipulator's end effector for each experiment. The left and right figures show x and y velocity versus position, respectively. Multiple trial trajectories are overlaid on each figure and these trajectories originate from the origin and terminate at red markers. Trials for which motion capture data was lost for a significant portion of time were omitted. This occurred when the end-effector endpoint was misinter-

preted as the ball center-point and is a limitation of the experimental setup. Raw end effector velocity measurements were filtered using a 5-point moving average, removing jitter from numerical differencing.

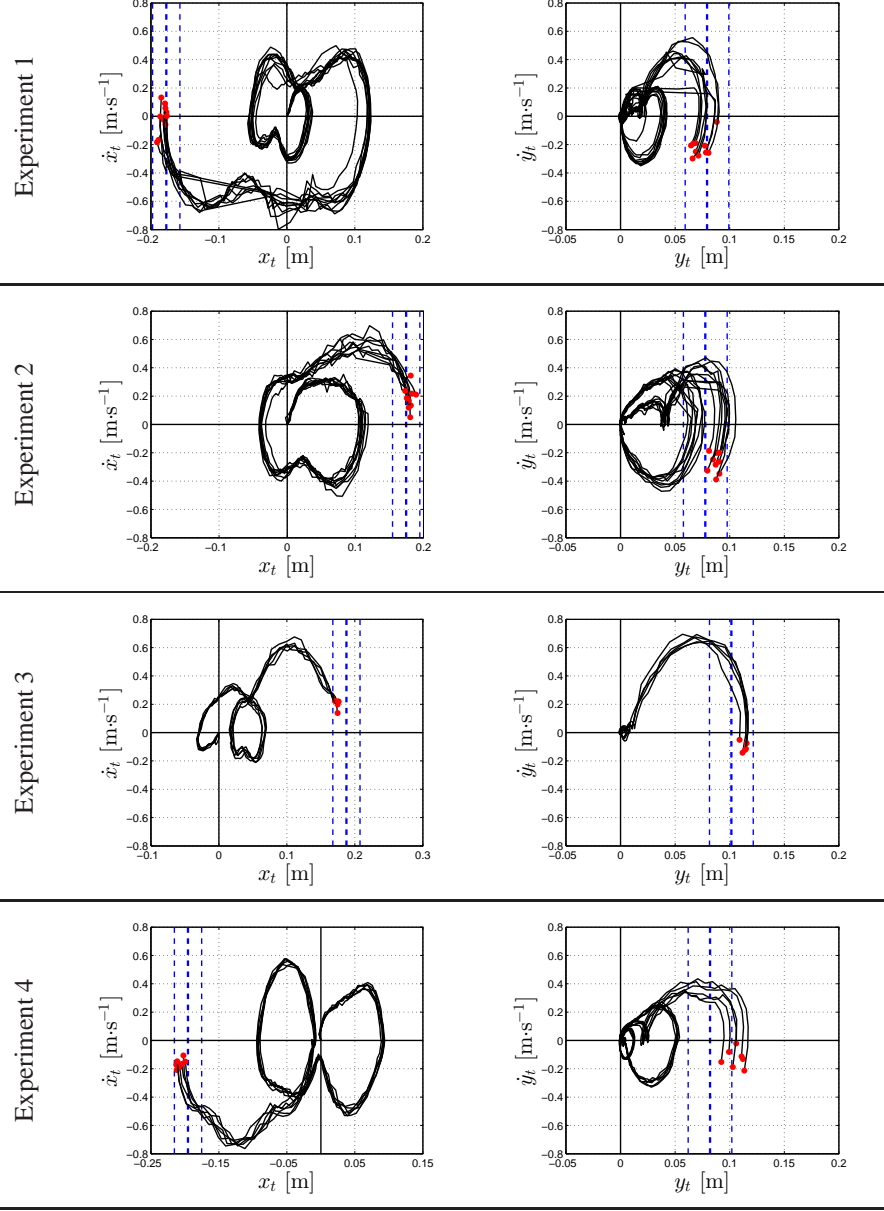


Figure 10: Cartesian state trajectories of the manipulator's end effector for each experiment. The left and right figures show x and y tip velocity versus position, respectively. The trajectories of independent trials for each experiment are overlaid in black. These trajectories originate from the origin and terminate at red markers indicating $t = t_f$. The vertical blue lines represent planned end-effector realizations ± 2 cm.

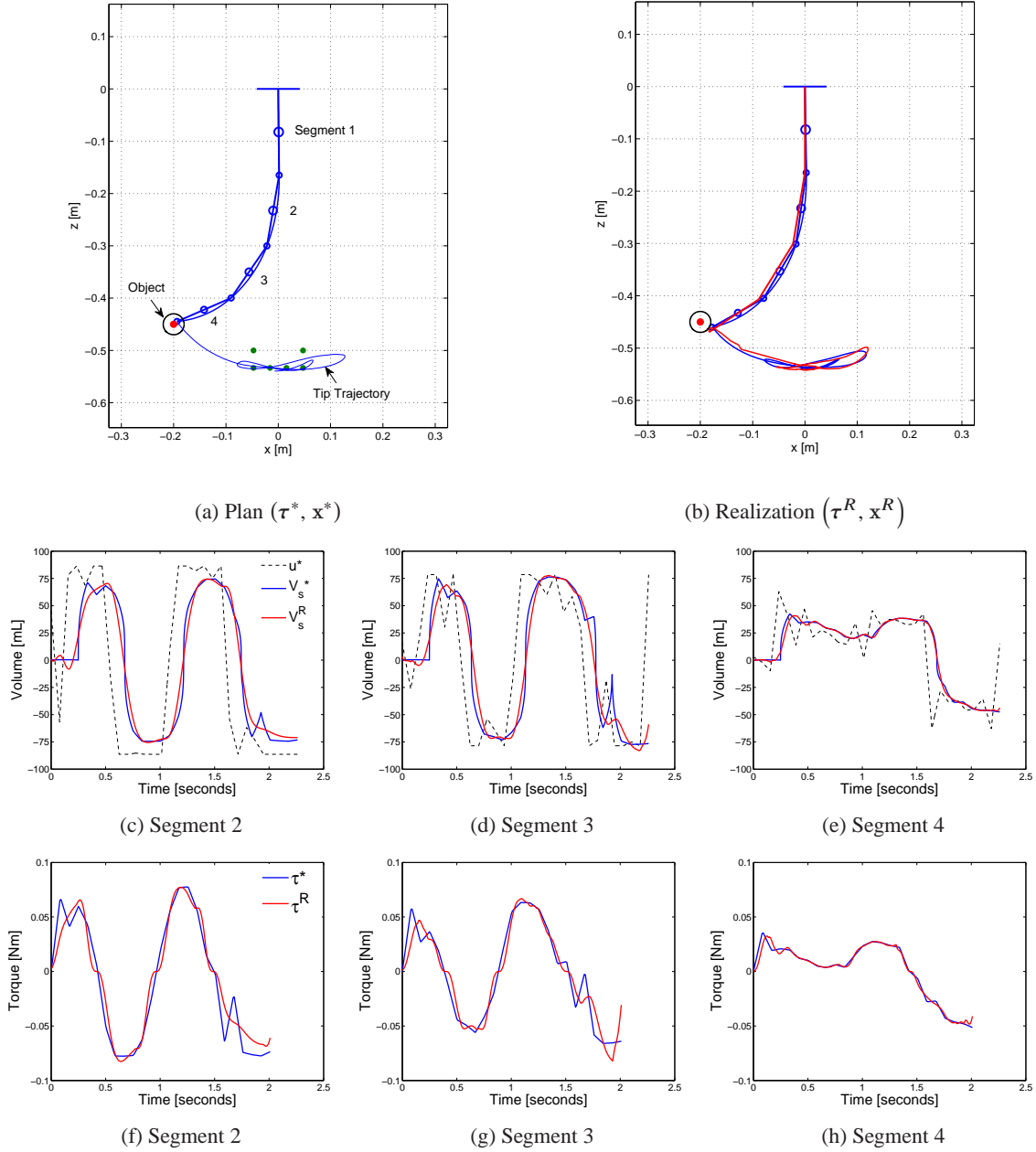
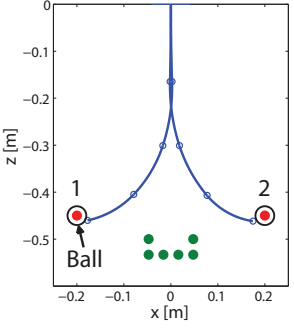
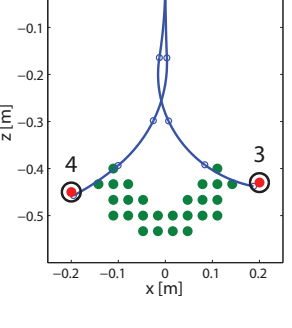


Figure 11: Experimental characterization of a dynamic *grab* maneuver performed with a four segment soft manipulator. Panels (a) and (b) depict the planned and realized manipulator motion in cartesian space respectively. In panel (a) the manipulator's predicted neutral axis is shown in blue and blue circles represent modeled center of mass locations. Here, green points represent a set of statically reachable points under estimated torque limits $|\tau| = [0.08, 0.07, 0.09, 0.13]^T$ and the red point represents the goal point of the maneuver. In (b) blue and red represent simulated and experimentally measured realizations of the ideal motion plan presented in (a). In panels (c)-(e) the locally optimal reference input trajectories u^* (dotted line), the target piston displacements V_s^* (blue line), and the realized piston displacements V_s^R (red line) are shown for segments 2, 3, and 4 respectively. Similarly, in panels (f)-(h) the locally optimal torque trajectories τ^* (blue) and realizations τ^R (red) are again shown for each actuated segment.

Table 3: Summary of Grabbing Experiments

Exp. #	Sys IDs	Consecutive Attempts	Successful Grabs	Plan Realization at $t = t_f$	
					
1	2	10	10		
2	0	10	9 [†]		
3	2	5	4 [*]		
4	1	12	11 [*]		

[†] Actuator burst during 10th attempt.

^{*} A successful grab occurred after the failed attempt.

6 Bracing

Static bracing is a motion primitive enabled by the development of an identified dynamic model for the soft manipulation system in Section 4. By understanding the system’s dynamics we can devise a planning algorithm that searches for and executes an environmental brace during a manipulation task. This is similar to the way humans rest their wrists against a table while writing. By statically bracing against nearby objects, we are able to ground the manipulator at a point between its base and end-effector, effectively reducing the contribution of dynamic forces and uncertainty from some number of manipulator segments on the primary manipulation task, e.g. end effector movement.

The concept of bracing for manipulation was first introduced in the 1980s [Book et al., 1985]. Bracing strategies with rigid body manipulators can involve physically fixing a distal point on the manipulator to a bracing surface (e.g. using suction, mechanical clamps, or magnets), but these approaches require additional hardware limiting the surfaces against which the manipulator can brace. Alternatively, normal force, or the component of contact force normal to the bracing surface, can be used to form braces as in Lew and Book [1994]. Here, a hybrid force-position controller is developed to mitigate the control complexity arising from normal force bracing. Despite the complexity, normal force bracing is a more universal strategy in that it only requires a suitable bracing surface to lie within the null space of the manipulator. Additionally, bracing strategies with probabilistic contact estimation [Petrovskaya et al., 2007] and multiple contact controllers [Park and Khatib, 2008] have been developed for rigid body manipulators. It is evident that for such manipulators contact force must be controlled to prevent damage to both the robot and the environment.

Here, we show that bracing is also a feasible and effective strategy for soft fluidic elastomer manipulators. With such a soft manipulator the required bracing force is generally small relative to that of a traditional rigid body manipulator for a

given task. For tasks requiring high bracing forces, a soft fluidic elastomer manipulator will safely undergo elastic deformation before the bracing surface for a wider range of surfaces than a more traditional manipulator.

6.1 Limitations

We do not provide a dynamic model that considers contact, nor do we have knowledge of the contact forces through sensing. Rather, the intent of this section is to show that the presented dynamic model and planning infrastructure is sufficient to accomplish simple normal force bracing at an arm segment’s endpoint. Specifically, we make the assumption that the piecewise constant curvature modeling assumption remains valid despite the kinematic constraints imposed by the brace.

6.2 Bracing Conditions

We outline three criteria for the static bracing strategy and these conditions help to illustrate the differences in employing this manipulation primitive with a soft elastomer robot as opposed to with a more traditional rigid body manipulator.

6.2.1 Condition 1

The contact force between the robot and object must be of sufficient magnitude to form a static brace. Figure 12 illustrates this concept. We assume the surface of the robot and the surface of the object come into contact and that they are non-moving. We can relate the normal force F_n , or the component of contact force normal to the bracing surface at $\hat{\mathbf{a}}$, the brace position and orientation, and the friction force F_f as

$$F_f \leq \mu_s F_n, \quad (32)$$

where μ_s is the static coefficient of friction between the two surfaces. Accordingly, $\mu_s F_n$ is the threshold below which the

robot's tangential force F_t will not break the static brace. That is,

$$F_t < \mu_s F_n. \quad (33)$$

Components of force due to end-effector interactions as well as due to the robot's actuators compose F_n and F_t .

In general, the soft fluidic elastomer robot presented in this work can statically brace with less contact force than a hard robot. The soft robot is composed of low durometer silicone rubber and this material has a high coefficient of static friction when in contact with solids [ToolBox]. During normal force bracing, a rigid body robot is coated with a wear resistant surface [Book et al., 1985], which has a low coefficient of static friction when in contact with solids [ToolBox]. For example, teflon in contact with steel has a μ_s of between 0.05 and 0.20 [ToolBox] whereas soft silicone rubber in contact with steel has a μ_s of between 0.6 and 0.9 [Mesa Múnera et al., 2011]. It follows that for a given tangential force F_t , a hard robot will have to exert a force on the object of between 3 and 18 times greater than a soft robot to maintain a static brace.

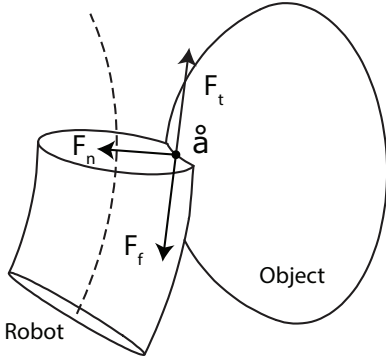


Figure 12: Illustration of normal force bracing where the first condition is that contact force between the robot and object must be of sufficient magnitude to form a static brace.

6.2.2 Condition 2

The normal force at the static brace point should not deform the object. The motivation behind this condition is that the robot should not damage the environment by bracing. Figure 13a schematically represents the local interaction between the robot and object. The normal force F_n radially compresses both the robot and the object, whose local stiffnesses are represented by k_R and k_O respectively. The condition can then be written as $k_O \gg k_R$. This relationship implies that the robot will deform well before the object deforms. For an entirely soft robot this condition is satisfied over a wider larger range of objects than for a rigid body manipulator with mechanical compliance. For example, Figure 13b depicts the radial stiffness, normal to the bending axis, of a robot made entirely of silicone rubber. The robot's radial stiffness is approximately $1 \frac{N}{mm}$. Additionally, the torsional stiffness between the base and brace point is approximately $0.2 \frac{N}{rad}$. To the best of our knowledge, the stiffness of a soft fluidic elastomer robot is

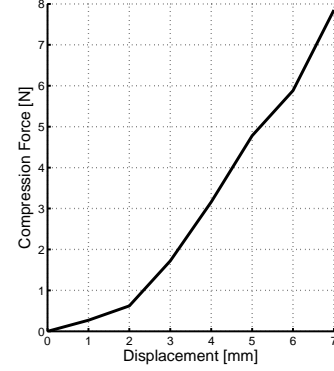
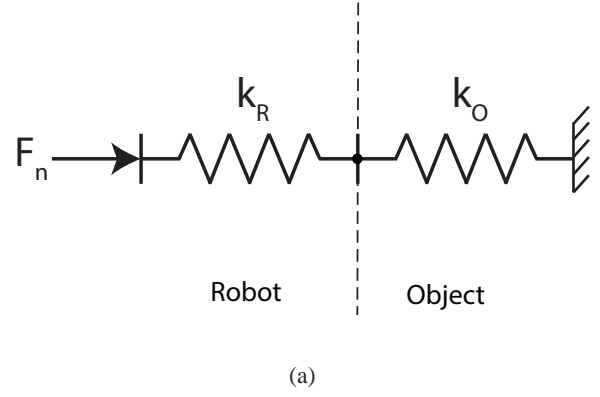


Figure 13: (a) A simplified model of the local interaction between the robot and object. (b) Radial stiffness, normal to the bending axis, of a robot made of silicone rubber.

lower than a rigid body manipulator with mechanical compliance.

6.2.3 Condition 3

There must exist a pose \hat{a} on and tangential to an object's surface O and a set of joint space parameters θ and γ such that the task space is contained within the workspace, or reachable envelope, of the manipulator and \hat{a} is within the nullspace.

Figure 14 illustrates the kinematic conditions for static bracing. Here the task space is shown as a square region, the bracing object O is shown as a sphere, and the soft robot is composed of multiple cylindrical bending segments.

6.3 Bracing Algorithm

Having outlined the conditions required for bracing, we next devise a planning algorithm that satisfies these conditions and allows the soft elastomer manipulator to execute an environmental brace. To begin, consider a soft manipulator whose dynamics can be represented in the manipulator form as outlined

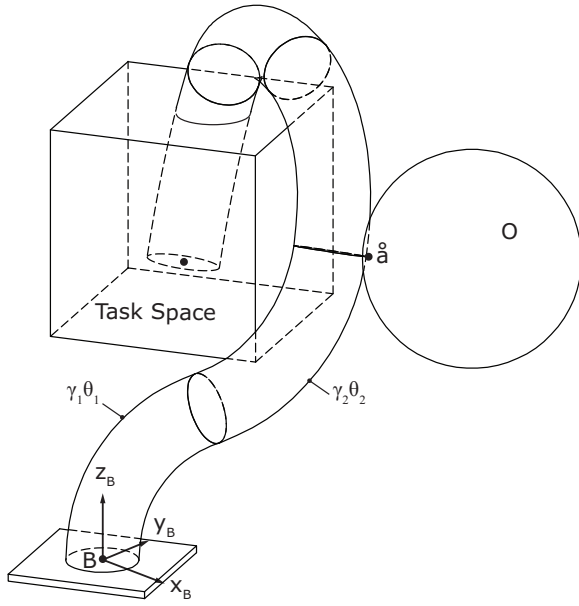


Figure 14: A depiction of the third kinematic condition for static bracing

in Section 3

$$\mathbf{H}(\theta) \ddot{\theta} + \mathbf{C}(\theta, \dot{\theta}) \dot{\theta} + \mathbf{G}(\theta) = \mathbf{B} \tau + \frac{\partial \phi}{\partial \theta} \lambda, \quad (34)$$

$$\phi(\theta) = 0, \quad (35)$$

where λ are external forces defined by static brace constraints. We propose finding a feasible static brace pose $\hat{\mathbf{a}}$ by solving the following optimization,

$$\min_{\tau, \theta, \gamma, \hat{\mathbf{a}}} \tau^T R \tau \leftarrow \text{Minimal Effort}$$

$$\begin{aligned} \text{subject to} \quad & \mathbf{G} - \frac{\partial \phi}{\partial \theta} \lambda - \mathbf{B} \tau = 0, \quad \leftarrow \text{Gravity and Contact Comp} \\ & \|\text{arm.FORKIN}_N(\theta, \gamma) - \text{Goal}\| = 0, \quad \leftarrow \text{Task} \\ & \|\text{arm.FORKIN}_{N-n}(\theta, \gamma) - \hat{\mathbf{a}}\| = 0, \quad \leftarrow \text{Brace Constraint} \\ & \tau_m^{\min} \leq \tau_m \leq \tau_m^{\max} \quad \forall m = 1 \dots M, \\ & \theta_n^{\min} \leq \theta_n \leq \theta_n^{\max} \quad \forall n = 1 \dots N, \\ & \gamma_n^{\min} \leq \gamma_n \leq \gamma_n^{\max}, \\ & \dot{\theta}_n = 0, \\ & \dot{\gamma}_n = 0. \end{aligned} \quad (36)$$

Algorithm 3 uses the optimization outlined in Equation 36 as well as a classical controller for each generalized coordinate of the soft arm to perform the primary task of positioning the manipulator's end effector while accomplishing the secondary task of bracing an intermediate segment's endpoint against a nearby surface if possible. For simplicity, we again operate within a sagittal plane defined by γ_1 and fix $\gamma_2 \dots \gamma_N = 0$. The task space is simply a *Goal* point in \mathbb{R}^3 .

Algorithm 3: Static Brace Strategy

```

n = 1.
while A feasible solution does not exist do
     $\theta^*, \hat{\mathbf{a}}^* \leftarrow$  Find an optimal static brace solution using (36) (refer to
        Section 6.2.3).
    n ++.
end
Move into contact with the object at  $\hat{\mathbf{a}}^*$  by servoing the proximal  $N - n$ 
segments to  $\theta_1^* \dots \theta_n^*$ .
Apply normal force to object (refer to Section 6.2.1).
Replan optimal solution for reaching goal using (36) with the added
constraints of  $\theta_1^* \dots \theta_n^*$  equaling the measured arc space configuration.

Move to goal by servoing the distal  $n$  segments to  $\theta_{n+1}^* \dots \theta_N^*$ .

```

6.4 Bracing Evaluations

6.4.1 Simulations

To evaluate the strategy of static bracing for a soft elastomer manipulator, we simulated Algorithm 3 on an identified model of the manipulator but with increased generalized input limits. The objective of the simulations is to demonstrate the formation of a simple environmental brace. The arm was servoed during steps 2 and 5 of the simulation using a PD controller for each arm segment. During step 3, we assume the arm is capable of satisfying Condition 1 without simulating the contact force, and in order to simulate the effect of contact we increase the friction, or damping coefficient, acting on the braced segments once the Brace Pose Constraint is satisfied. The results of the simulation are shown in Figures 15. The top 3 panels of Figure 15 show an example of a static brace formed at the endpoint of the second link of a four link manipulator. The left panel illustrate steps 1 through 3 of Algorithm 3 occurring over 5 seconds. Here, the black circle represents the object, the blue curves represent the neutral axis of the 4-link soft manipulator overlaid at one second intervals, and the small red circle represents the goal location of the end effector. The center panel illustrates steps 4 and 5 of Algorithm 3 where the manipulator executes its primary task of moving the end effector to the goal. The neutral axes are overlaid at 0.5 second intervals. The right panel depicts the arm moving to the goal location in the absence of a nearby object, where a brace strategy is not feasible.

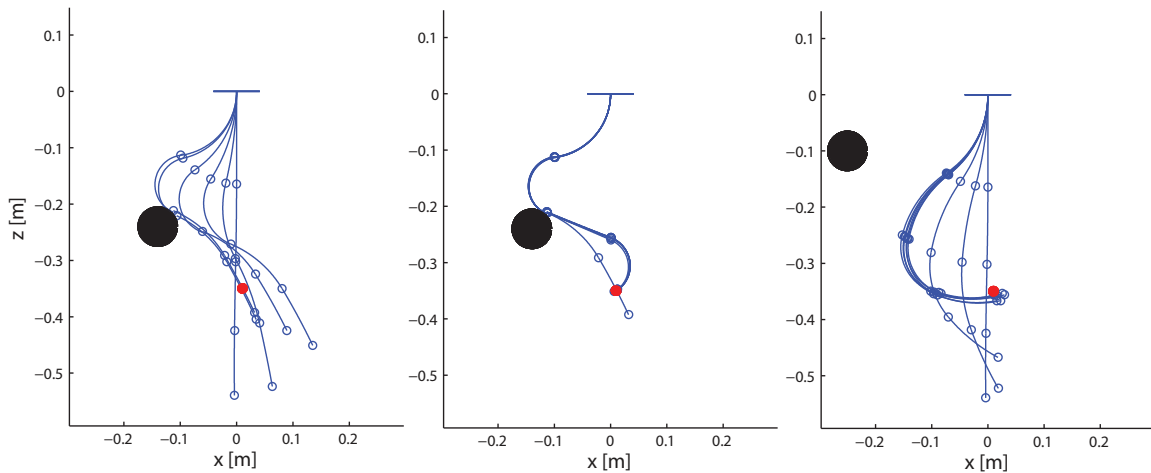


Figure 15: Simulation of static bracing with a soft elastomer manipulator. Left panel: Steps 1 through 3 of Algorithm 3 are illustrated. Here, the black circle represents the object, the blue curves represent the neutral axis of the 4-link soft manipulator overlaid at one second intervals, and the small red circle represents the goal location of the end effector. Center Panel: Steps 4 and 5 of Algorithm 3 are illustrated. Here, the manipulator executes its primary task of moving its end effector to the red goal location. The neutral axes are overlaid at 0.5 second intervals. Right Panel: A depiction of the arm moving to the goal location in the absence of a nearby object, where a brace strategy is not feasible.

7 Conclusion

An approach for dynamically controlling soft robots is explored. First, a dynamic model for a soft fluidic elastomer manipulator is developed. Then, a method for identifying all unknown system parameters is presented, i.e. the soft manipulator, fluidic actuators, and continuous drive cylinders. Using this identified model and trajectory optimization routines, locally-optimal dynamic maneuvers called *grabs* are planned through iteration learning control and repeatably executed on a physical prototype. Actuation limits, the self-loading effects of gravity, and the high compliance of the manipulator, physical phenomena common among soft robots, are represented as constraints within the optimization. Additionally, we present the idea of bracing for soft robots. We outline conditions for static environmental bracing and develop an algorithm for planning a brace. Experimentally, we validate this concept by comparing braced and unbraced end-effector motions.

In these initial experiments, we found it feasible to compute a sufficiently accurate dynamic model to make planning viable for a soft elastomer manipulator. However, to obtain the required performance for executing specific tasks, like grabbing, we found it necessary to use iterative learning control. In future work, these trajectories may be stabilized using linear time-varying linear quadratic regulators (LTV LQRs) [Tedrake, 2009] making them robust to uncertainty in initial conditions and tolerant of modeling inaccuracies. Additionally, more accurate dynamic models may need to be developed. Although this class of robot is well-suited for environmental contact (e.g. whole arm grasping and bracing), the modeling assumptions used here may not suffice under these conditions. Specifically, the dynamic model presented here does not consider contact. Further, only the fundamentals of bracing are explored in this paper. It is likely that bracing may enable a

wide variety of capabilities for soft elastomer machines and we intended this work to begin that discussion. Also, during grab experiments, hook and loop fasteners were used on the manipulators end effector and the ball. To some degree, this mechanism compensated for positional errors as the ball and end effector were securely connected after the moment of contact. This work suggests dynamic model-based planning and control may be an appropriate approach for soft robotics.

Acknowledgments

This work was done in the Distributed Robotics Laboratory at MIT with support from the National Science Foundation, grant numbers NSF 1117178, NSF IIS1226883, and NSF CCF1138967 as well as the NSF Graduate Research Fellowship Program, primary award number 1122374. We are grateful for this support. The authors declare no competing financial interests.

Appendix A: Index to Multimedia Extensions

Extension	Type	Description
1	Video	This video demonstrates the soft fluidic elastomer manipulator prototype executing locally-optimal open loop policies found using an iterative learning control algorithm.

References

- Wayne J Book, Sanh Le, and Viboon Sangveraphunsiri. Bracing strategy for robot operation. In *Theory and Practice of Robots and Manipulators*, pages 179–185. Springer, 1985.
- David Braganza, Darren M Dawson, Ian D Walker, and Niten-dra Nath. A neural network controller for continuum robots. *Robotics, IEEE Transactions on*, 23(6):1270–1277, 2007.
- Marcello Calisti, Andrea Arienti, Maria Elena Giannaccini, Maurizio Follador, Michele Giorelli, Matteo Cianchetti, Barbara Mazzolai, Cecilia Laschi, and Paolo Dario. Study and fabrication of bioinspired octopus arm mockups tested on a multipurpose platform. In *Biomedical Robotics and Biomechatronics (BioRob), 2010 3rd IEEE RAS and EMBS International Conference on*, pages 461–466. IEEE, 2010.
- Marcello Calisti, Michele Giorelli, Guy Levy, Barbara Mazzolai, B Hochner, Cecilia Laschi, and Paolo Dario. An octopus-bioinspired solution to movement and manipulation for soft robots. *Bioinspiration & biomimetics*, 6(3): 036002, 2011.
- Gang Chen, Minh Tu Pham, and Tanneguy Redarce. Development and kinematic analysis of a silicone-rubber bending tip for colonoscopy. In *Intelligent Robots and Systems, 2006 IEEE/RSJ International Conference on*, pages 168–173, 2006. doi: 10.1109/IROS.2006.282129.
- Gregory S Chirikjian. Hyper-redundant manipulator dynamics: a continuum approximation. *Advanced Robotics*, 9(3): 217–243, 1994.
- Gregory S Chirikjian and Joel W Burdick. Kinematically optimal hyper-redundant manipulator configurations. *Robotics and Automation, IEEE Transactions on*, 11(6):794–806, 1995.
- Matteo Cianchetti, Tommaso Ranzani, Giada Gerboni, Iris De Falco, Cecilia Laschi, and Arianna Menciassi. Stiff-flop surgical manipulator: Mechanical design and experimental characterization of the single module. In *Intelligent Robots and Systems (IROS), 2013 IEEE/RSJ International Conference on*, pages 3576–3581, Nov 2013. doi: 10.1109/IROS.2013.6696866.
- Nikolaus Correll, Cagdas D. Onal, Haiyi Liang, Erik Schoenfeld, and Daniela Rus. Soft autonomous materials - using active elasticity and embedded distributed computation. In *12th Internatoinal Symposium on Experimental Robotics*, New Delhi, India, 2010.
- Raphael Deimel and Oliver Brock. A compliant hand based on a novel pneumatic actuator. In *Robotics and Automation (ICRA), 2013 IEEE International Conference on*, pages 2047–2053, May 2013. doi: 10.1109/ICRA.2013.6630851.
- Ian A Gravagne and Ian D Walker. Uniform regulation of a multi-section continuum manipulator. In *Robotics and Automation, 2002. Proceedings. ICRA’02. IEEE International Conference on*, volume 2, pages 1519–1524. IEEE, 2002.
- Ian A Gravagne, Christopher D Rahn, and Ian D Walker. Large deflection dynamics and control for planar continuum robots. *Mechatronics, IEEE/ASME Transactions on*, 8(2): 299–307, 2003.
- Michael W Hannan and Ian D Walker. Kinematics and the implementation of an elephant’s trunk manipulator and other continuum style robots. *Journal of Robotic Systems*, 20(2): 45–63, 2003.
- Bryan A Jones and Ian D Walker. Kinematics for multisection continuum robots. *Robotics, IEEE Transactions on*, 22(1): 43–55, 2006a.
- Bryan A Jones and Ian D Walker. Practical kinematics for real-time implementation of continuum robots. *Robotics, IEEE Transactions on*, 22(6):1087–1099, 2006b.
- Robert K Katzschnmann, Andrew D Marchese, and Daniela Rus. Hydraulic autonomous soft robotic fish for 3d swimming. In *International Symposium on Experimental Robotics (ISER)*, 2014.
- Cecilia Laschi, Matteo Cianchetti, Barbara Mazzolai, Laura Margheri, Maurizio Follador, and Paolo Dario. Soft robot arm inspired by the octopus. *Advanced Robotics*, 26(7): 709–727, 2012.
- Jae Young Lew and W.J. Book. Bracing micro/macro manipulators control. In *Robotics and Automation, 1994. Proceedings., 1994 IEEE International Conference on*, pages 2362–2368 vol.3, May 1994.
- Yu Lianzhi, Lu Yuesheng, Hu Zhongying, and Cheng Jian. Electro-pneumatic pressure servo-control for a miniature robot with rubber actuator. In *Digital Manufacturing and Automation (ICDMA), 2010 International Conference on*, volume 1, pages 631 –634, 2010. doi: 10.1109/ICDMA.2010.158.
- Ming Luo, Mahdi Agheli, and Cagdas D Onal. Theoretical modeling and experimental analysis of a pressure-operated soft robotic snake. *Soft Robotics*, 1(2):136–146, 2014.
- Andrew D Marchese and Daniela Rus. Design, kinematics, and control of a soft spatial fluidic elastomer manipulator. In *International Journal of Robotics Research*, 2015. (In press).
- Andrew D Marchese, Cagdas D Onal, and Daniela Rus. Soft robot actuators using energy-efficient valves controlled by electropermanent magnets. In *Intelligent Robots and Systems (IROS), 2011 IEEE/RSJ International Conference on*, pages 756–761. IEEE, 2011.
- Andrew D Marchese, Robert K Katzschnmann, and Daniela Rus. Whole arm planning for a soft and highly compliant 2d robotic manipulator. In *Intelligent Robots and Systems (IROS 2014), 2014 IEEE/RSJ International Conference on*, pages 554–560. IEEE, 2014a.

- Andrew D Marchese, Konrad Komorowski, Cagdas D Onal, and Daniela Rus. Design and control of a soft and continuously deformable 2d robotic manipulation system. In *Robotics and Automation (ICRA), 2014 IEEE International Conference on*, pages 2189–2196. IEEE, 2014b.
- Andrew D Marchese, Cagdas D Onal, and Daniela Rus. Autonomous soft robotic fish capable of escape maneuvers using fluidic elastomer actuators. *Soft Robotics*, 1(1):75–87, 2014c.
- Andrew D Marchese, Robert K Katzschmann, and Daniela Rus. A recipe for soft fluidic elastomer robots. *Soft Robotics*, 2(1):7–25, 2015a.
- Andrew D Marchese, Russ Tedrake, and Daniela Rus. Dynamics and trajectory optimization for a soft spatial fluidic elastomer manipulator. In *Robotics and Automation (ICRA), 2015 IEEE International Conference on*. IEEE, 2015b.
- Ramses V Martinez, Jamie L Branch, Carina R Fish, Lihua Jin, Robert F Shepherd, Rui Nunes, Zhigang Suo, and George M Whitesides. Robotic tentacles with three-dimensional mobility based on flexible elastomers. *Advanced Materials*, 25(2):205–212, 2013.
- William McMahan, Bryan A Jones, and Ian D Walker. Design and implementation of a multi-section continuum robot: Air-octor. In *Intelligent Robots and Systems, 2005.(IROS 2005). 2005 IEEE/RSJ International Conference on*, pages 2578–2585. IEEE, 2005.
- William McMahan, V Chitrakaran, M Csencsits, D Dawson, Ian D Walker, Bryan A Jones, M Pritts, D Dienno, M Grisom, and Christopher D Rahn. Field trials and testing of the octarm continuum manipulator. In *Robotics and Automation, 2006. ICRA 2006. Proceedings 2006 IEEE International Conference on*, pages 2336–2341. IEEE, 2006.
- Elizabeth Mesa Múnera et al. *Characterization of brain tissue phantom using an indentation device and inverse finite element parameter estimation algorithm*. PhD thesis, Universidad Nacional de Colombia, Sede Medellín, 2011.
- Hiromi. Mochiyama and Takahiro. Suzuki. Dynamical modelling of a hyper-flexible manipulator. In *SICE 2002. Proceedings of the 41st SICE Annual Conference*, volume 3, pages 1505–1510 vol.3, Aug 2002. doi: 10.1109/SICE.2002.1196530.
- Cagdas D Onal and Daniela Rus. Autonomous undulatory serpentine locomotion utilizing body dynamics of a fluidic soft robot. *Bioinspiration & biomimetics*, 8(2):026003, 2013.
- Cagdas D Onal, Xin Chen, George M Whitesides, and Daniela Rus. Soft mobile robots with on-board chemical pressure generation. In *International Symposium on Robotics Research (ISRR)*, 2011.
- Jaeheung Park and Oussama Khatib. Robot multiple contact control. *Robotica*, 26(5):667–677, 2008.
- Anna Petrovskaya, Jaeheung Park, and Oussama Khatib. Probabilistic estimation of whole body contacts for multi-contact robot control. In *Robotics and Automation, 2007 IEEE International Conference on*, pages 568–573, April 2007.
- Graham Robinson and John Bruce C. Davies. Continuum robots-a state of the art. In *Robotics and Automation, 1999. Proceedings. 1999 IEEE International Conference on*, volume 4, pages 2849–2854. IEEE, 1999.
- Robert F Shepherd, Filip Ilievski, Wonjae Choi, Stephen A Morin, Adam A Stokes, Aaron D Mazzeo, Xin Chen, Michael Wang, and George M Whitesides. Multigait soft robot. *Proceedings of the National Academy of Sciences*, 108(51):20400–20403, 2011.
- Robert F Shepherd, Adam A Stokes, Jacob Freake, Jabulani Barber, Phillip W Snyder, Aaron D Mazzeo, Ludovico Cademartiri, Stephen A Morin, and George M Whitesides. Using explosions to power a soft robot. *Angewandte Chemie*, 125(10):2964–2968, 2013.
- Joseph M Snyder and James F Wilson. Dynamics of the elastica with end mass and follower loading. *Journal of applied mechanics*, 57(1):203–208, 1990.
- Enver Tatlicioglu, Ian D Walker, and Darren M Dawson. Dynamic modelling for planar extensible continuum robot manipulators. In *Robotics and Automation, 2007 IEEE International Conference on*, pages 1357–1362. IEEE, 2007.
- Russ Tedrake. LQR-trees: Feedback motion planning on sparse randomized trees. In *Proceedings of Robotics: Science and Systems*, Seattle, USA, June 2009.
- Russ Tedrake. Drake: A planning, control, and analysis toolbox for nonlinear dynamical systems, 2014. URL <http://drake.mit.edu>.
- Michael T Tolley, Robert F Shepherd, Michael Karpelson, Nicholas W Bartlett, Kevin C Galloway, Michael Wehner, Rui Nunes, George M Whitesides, and Robert J Wood. An untethered jumping soft robot. In *Intelligent Robots and Systems (IROS 2014), 2014 IEEE/RSJ International Conference on*, pages 561–566. IEEE, 2014a.
- Michael T Tolley, Robert F Shepherd, Bobak Mosadegh, Kevin C Galloway, Michael Wehner, Michael Karpelson, Robert J Wood, and George M Whitesides. A resilient, untethered soft robot. *Soft Robotics*, 2014b. ahead of print.
- The Engineering ToolBox. Friction and coefficients of friction. URL http://www.engineeringtoolbox.com/friction-coefficients-d_778.html. Accessed: 2010-07-29.
- Deepak Trivedi, Christopher D Rahn, William M Kier, and Ian D Walker. Soft robotics: Biological inspiration, state of the art, and future research. *Applied Bionics and Biomechanics*, 5(3):99–117, 2008.

- Takuya Umedachi, Vishesh Vikas, and Barry A Trimmer. Highly deformable 3-d printed soft robot generating inching and crawling locomotions with variable friction legs. In *Intelligent Robots and Systems (IROS), 2013 IEEE/RSJ International Conference on*, pages 4590–4595, Nov 2013. doi: 10.1109/IROS.2013.6697016.
- Oskar von Stryk. Numerical solution of optimal control problems by direct collocation. In R. Bulirsch, A. Miele, J. Stoer, and K. Well, editors, *Optimal Control*, volume 111 of *ISNM International Series of Numerical Mathematics*, pages 129–143. Birkhuser Basel, 1993.
- Shuichi Wakimoto, Keiko Ogura, Koichi Suzumori, and Yasutaka Nishioka. Miniature soft hand with curling rubber pneumatic actuators. In *Robotics and Automation, 2009. ICRA '09. IEEE International Conference on*, pages 556–561, May 2009. doi: 10.1109/ROBOT.2009.5152259.
- Robert J Webster and Bryan A Jones. Design and kinematic modeling of constant curvature continuum robots: A review. *The International Journal of Robotics Research*, 29 (13):1661–1683, 2010.
- James F Wilson and Joseph M Snyder. The elastica with end-load flip-over. *Journal of applied mechanics*, 55(4):845–848, 1988.
- Jing Xiao and Rayomand Vatcha. Real-time adaptive motion planning for a continuum manipulator. In *Intelligent Robots and Systems (IROS), 2010 IEEE/RSJ International Conference on*, pages 5919–5926. IEEE, 2010.